Shangguan, Y., *et al.*: Large-Scaled Simulation on the Coherent Vortex ...
THERMAL SCIENCE: Year 2015, Vol. 19, No. 3, pp. 977-988

977

LARGE-SCALED SIMULATION ON THE COHERENT VORTEX EVOLUTION OF A JET IN A CROSS-FLOW BASED ON LATTICE BOLTZMANN METHOD

by

Yanqin SHANGGUAN, Xian WANG, and Yueming LI*

State Key Laboratory for Strength and Vibration of Mechanical Structures, School of Aerospace,
Xi´an Jiaotong University, Xi´an, Shaanxi, China

Large eddy simulation is performed on a jet issued normally into a cross-flow using lattice Boltzmann method and multiple graphic processing units (multi-GPU) to study the flow characteristics of jets in cross-flow. The simulation with $1.50 \cdot 10^8$ grids is fulfilled with 6 K20M GPU. With large-scaled simulation, the secondary and tertiary vortices are captured. The features of the secondary vortices and the tertiary vortices reveal that they have a great impact on the mixing between jet flow and cross-flow. The qualitative and quantitative results also indicate that the evolution mechanism of vortices is not constant, but varies with different situations. The hairpin vortex under attached jet regime originates from the boundary layer vortex of cross-flow. While, the origin of hairpin vortex in detached jet is the jet shear-layer vortex. The mean velocities imply the good ability of lattice Boltzmann method to simulate jet in a cross-flow and the large loss of jet momentum in detached jet caused by the strong penetration. Besides, in our computation, a high computational performance of 1083.5 MLUPS is achieved.

Key words: *jet in a cross-flow, coherent structures, evolution mechanism, lattice Boltzmann method, multiple graphic processing units*

Introduction

Jet in a cross-flow (JICF), also called transverse jets, is a basic flow which seems simple but complicated. It is evident that the applications of JICF extend throughout many engineering fields, therefore it has triggered numerous flow studies over the past 50 years [1-4]. A large number of experimental and numerical investigations were carried out to study all kinds of JICF features, such as velocity distribution, mixing intensity, formation mechanism of vortex, and so on. Among them, the coherent structures in JICF is one of the focuses. Because it is the result of interaction between jet flow and cross-flow, which plays an significant role in mixing and dispersion, *etc*.

Although a considerable number of studies have dealt with the coherent structures in JICF, unanimous agreements have not yet to be reached on the formation and evolution mechanisms of different vortices. Because JICF is a three-dimensional flow associated with high complexity, and a precise study to obtain the exact understanding of vortical structures in JICF is

---

* Corresponding author; e-mail: wangxian@mail.xjtu.edu.cn

necessary. In spite of lots of experiments on JICF were conducted with various precision measurement devices, it is still extremely difficult to get the very detailed data on flow characteristics via experiment. Hence the computational study of JICF with fine resolution is indispensible for an in-depth study on JICF.

To study JICF clearly and capture the coherent structures as fine as possible, the resolution of grid system is important. However, it is still a bottleneck problem due to the limitation of computational tools. To the best of our current knowledge, few numerical studies of JICF were performed with over one hundred million computational grids. CFD predictions of wake-stabilised jet flames in a cross-flow were carried out by Lawal *et al.* [5] with the total mesh number of $1.2 \cdot 10^6$. Brinkerhoff *et al.* [6] performed a direct numerical simulation (DNS) of a square jet ejected transversely into a laminar boundary-layer flow using about $6.3 \cdot 10^6$ meshes. Duda *et al.* [7] fulfilled the scale-adaptive simulation on a hot jet in cross-flow with $1.31 \cdot 10^7$ computational grids. In 2013, Andrew *et al.* [8] performed a blind large eddy simulation (LES) of film-cooling, the application of JICF, with $8.87 \cdot 10^7$ grid points. This is by far the most massive computational grid system in our minds, and it was run on 256 processors (8 nodes of quad-processor eight-core 2.0 GHz AMD Opteron 6128), 512 GB ram, and a 20 Gb/s infiniband interconnect. It took about 2 months to perform this simulation and a computational performance of 3.5 MLUPS was obtained.

In recent years, lattice Boltzmann method (LBM), one of the meso-scale methods, has developed fast and been regarded as a promising alternative for complex fluid-flows simulation. A lot of numerical investigations based on LBM have been conducted and got exact results in the past few years [9-11]. Because it is of advantages, such as, easy implementation of boundary conditions, easy programming, and fully parallel algorithms [12]. In particular, its fully parallel algorithms make it match perfectly with graphic processing unit (GPU) which has super computing power [13]. Therefore, it is easy and efficient to fulfill large-scaled simulations by using LBM and GPU.

Aiming at capturing the fine coherent structures to understand the exact characteristics of vortical structures in JICF, we attempt to study three-dimensional JICF with a large-scaled simulation based on LBM and using multiple GPU (multi-GPU). The jet is injected perpendicularly into the cross-flow and the Reynolds number based on cross-flow velocity and jet diameter is $\text{Re} = (\rho u_\infty D)/v = 2400$. The blowing ratios $BR = (\rho_j u_j)/(\rho_\infty u_\infty)$ are set as 0.25 and 3.31 to study the features of vortical structures under attached and detached jet regimes. The simulations are carried out in a parallelized way on 6 K20M GPU with MPI-CUDA.

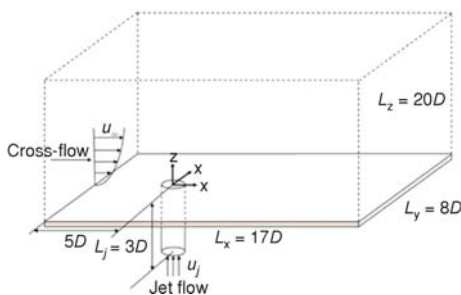## Flow configuration and computation details

Figure 1. Flow configuration

The present computation is set to correspond with an experimental research of an idealized round jet in a cross-flow carried out by Ozcan *et al.* [14]. Figure 1 shows the flow configuration used in this computation. The dimensions of the domain are $17D$ in streamwise (x) direction, $8D$ in spanwise (y) direction, and $8D$ in wall-normal (z) direction, respectively. The origin of the co-ordinate system is situated at the center of the jet hole, which locates in the mid-span plane and $5D$ downstream from the inlet of the cross-flow. The length of the jet pipe is

set as $L_j = 3D$. 44 grid points are fixed for the length of $1D$, resulting in that the total mesh number is about $1.50 \cdot 10^8$. For the considered case, the jet is discharged perpendicularly into the cross-flow. The Reynolds number is $Re = 2400$. Two blowing ratios of $BR = 0.25, 3.31$ are considered.

All the simulations presented in this paper are performed with uniform grid. To obtain the time-averaged statistics, the flow field has been sampled over 10 throw-time (T). Here, one throw-time T based on the cross-flow velocity u_∞ is the time which the cross-flow takes to pass over the whole of the bottom plate.

Numerical method

Lattice Boltzmann equation (LBE) formulation for large eddy simulation

In LBM, the following Boltzmann equation for the discrete velocity distribution is solved on a discrete lattice [15]:

$$\frac{\partial f_i}{\partial t} + \vec{e}_i \cdot \nabla f_i = \Omega_i \, (i = 1, 2, ..., N) \tag{1}$$

where f_i is the particle velocity distribution function, $\vec{e}_i$ – the particle velocity in the ith direction, and N – the number of velocities. For 3D model, there are several cubic lattice models, such as D3Q13, D3Q15, D3Q19, and D3Q27 ($N = 13, 15, 19$ or 27). Ω_i is the collision operator. Using Boltzmann-BGK approximation [16]:

$$\Omega_i = -\frac{1}{\lambda}(f_i - f_i^{eq}) \tag{2}$$

then we get

$$\frac{\partial f_i}{\partial t} + \vec{e}_i \cdot \nabla f_i = -\frac{1}{\lambda}(f_i - f_i^{eq}) \tag{3}$$

where, f_i^{eq} is the local equilibrium distribution, and λ – the relaxation time. To obtain the Navier-Stokes equations, the equilibrium distribution functional form must be carefully chosen. In the 13-speed square lattice and 15, 19, 27-speed cubic lattices, a suitable equilibrium distribution function has been proposed as:

$$f_i^{eq} = \rho \varpi_i \left[1 + 3\vec{e}_i \cdot \vec{u} + \frac{9}{2}(\vec{e}_i \cdot \vec{u})^2 - \frac{3}{2}\vec{u} \cdot \vec{u} \right] \tag{4}$$

In the present study, D3Q19 model shown in fig. 2 is adopted. The corresponding weighting factors are $\varpi_0 = 1/3$, $\varpi_1 \sim \varpi_6 = 1/18$ and $\varpi_7 \sim \varpi_{18} = 1/36$. ρ and $\vec{u}$ are the macroscopic quantities and can be evaluated as:

$$\rho = \sum_{i=0}^{N} f_i = \sum_{i=0}^{N} f_i^{eq} \tag{5}$$

$$\rho\vec{u} = \sum_{i=0}^{N} f_i \vec{e}_i = \sum_{i=0}^{N} f_i^{eq} \tag{6}$$

The speed of sound is $c_s = 1/(3)^{1/2}$, and the ideal-gas state equation is:
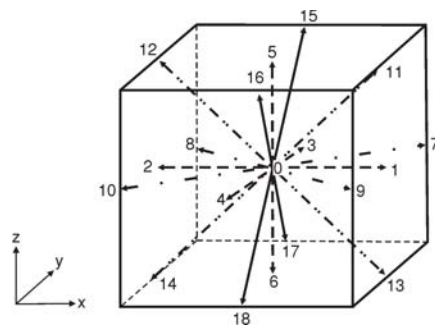

Figure 2. D3Q19 LBM model

$$p = \rho c_s^2 = \frac{\rho}{3} \tag{7}$$

The completely discretized form of eq. (3) is:

$$f_i(\vec{x} + \vec{e}_i \delta t, t + \delta t) - f_i(\vec{x}, t) = -\frac{1}{\tau}[f_i(\vec{x}, t) - f_i^{eq}(\vec{x}, t)] \tag{8}$$

Equation (8) is the well known LBGK model, where, $t = \lambda/\delta t$ is the non-dimensional relaxation time. The viscosity in macroscopic Navier-Stokes equation can be derived from eq. (8) as:

$$v = \left(\tau - \frac{1}{2}\right)\delta t \tag{9}$$

Equation (8) is usually solved with its standard form by assuming and according to the following two steps:

– collision step $\qquad \widetilde{f}_i(\vec{x}, t) = f_i(\vec{x}, t) - \frac{1}{\tau}[f_i(\vec{x}, t) - f_i^{eq}(\vec{x}, t)] \tag{10}$

– streaming step $\qquad\qquad f_i(\vec{x} + \vec{e}_i, t + 1) = \widetilde{f}_i(\vec{x}, t) \tag{11}$

where f_i and $\widetilde{f}_i$ denote the pre- and post-collision states of the distribution function, respectively.

As for the LES, the filtered form of the LBE for LES is defined as [17, 18]:

$$\widetilde{f}_i(x + e_i \delta t, \ t + \delta t) = \bar{f}_i(x, \delta t) - \frac{1}{\tau_*}[\bar{f}_i - \bar{f}_i^{eq}] \tag{12}$$

$$\tau_* = \tau_0 + \tau_i \tag{13}$$

where $\bar{f}_i$ and $\bar{f}_i^{eq}$ represent the distribution function and the equilibrium distribution function of the resolved scales, respectively. Moreover, τ_0 and τ_i, respectively, are the relaxation time corresponding to the molecular viscosity v_0 and eddy viscosity v_t. Accordingly, v_* is given as [17, 18]:

$$v_* = v_0 + v_t = \frac{1}{3}\left(\tau_* - \frac{1}{2}\right)c^2\delta t \tag{14}$$

$$v_0 = \frac{1}{3}\left(\tau_0 - \frac{1}{2}\right)c^2\delta t, \ v_t = \frac{1}{3}\tau_t c^2\delta t \tag{15}$$

The eddy viscosity v_t arising from the standard Smagorinsky model can be calculated with the filter length scale Δ_x and the filtered strain rater tensor $\bar{S}_{ij} = (\partial_j \bar{u}_i + \partial_i \bar{u}_j)/2$.

$$v_t = (C_S \Delta_x)^2 \bar{S}, \bar{S} = \sqrt{2\sum_{ij} \bar{S}_{ij} \bar{S}_{ij}} \tag{16}$$

here, C_S is Smagorinsky constant and is set as $C_S = 0.13$ according to our previous study [19]. Based on the opinion of Bardina *et al.* [20], the value of LES filter length scale is $\Delta_x = (3)^{1/2}$ in LBM. To be prudent, we choose $\Delta_x = 1$ in this paper.

Boundary conditions

As for the boundary conditions, periodic boundary condition is applied on the two boundaries in spanwise direction. A 1/7 power law velocity profile is adopted at the inlet of cross-flow. This cross-flow inlet profile assumes a turbulent boundary layer thickness of $\delta = 2.9D$, which is the

same as that was measured in the experiment [14], and a cross-flow free-stream velocity of u_∞. Flow-out BC is set for exit. A non-equilibrium extrapolation boundary condition is used for non-slip static bottom plate and top boundary:

$$\widetilde{f}_i = f_i^{\ eq} + f_i^{\ neq} = f_i^{\ eq} + f_{i\_neighbor}^{\ neq} = f_i^{\ eq} + (\widetilde{f}_{i\_\text{neighbor}} - f_{i\_neighbor}^{\ eq}) \tag{17}$$

where $f_i^{\ eq}$ is computed by the macroscopic values $\vec{u}$ and ρ on the boundaries according to eq. (4). $f_i^{\ neq}$ can not be computed directly and is assumed to be equal to the value of its neighboring inner node $f_{i\_neighbor}^{\ neq}$, $\widetilde{f}_{i\_neighbor}$, and $f_{i\_neighbor}^{\ eq}$ are computed by eq. (10) and eq. (4), respectively, with the corresponding $\vec{u}$ and ρ.

Results and discussion

Performance of computation by GPU

The present parallel computation is made by one-dimensional domain partitioning using 6 K20M GPU, which are equipped in 2 nodes, *i. e.* 3GPU per node. The network connection abide by the TCP/IP transport protocol. As for detailed information on data transfer, interested readers could refer to the paper of Wang and Aoki [21].

For current simulation, it takes about 6 hours to simulate $1.563 \cdot 10^6$ LBM-steps, 20 times of throw-time *T*, for $1.50 \cdot 10^8$ LBM-grids with 6 K20M GPU. The performance achieves 1083.5 MLUPS, that is $1.8035 \cdot 10^9$ meshes are processed per second.

The evolution mechanism of vortical structures in JICF

The primary coherent structures in JICF are the hairpin vortex, the horseshoe vortex, the upright wake vortex, and the jet shear-layer vortex. Most of these structures have been identified experimentally and the flow structures have been visualized by using smoke-wire or dye-injection techniques [22, 23]. The *Q*-criterion is chosen as a vortex-identification method to identify the coherent structures in this paper. The *Q*-criterion was named after the second invariant of velocity gradient tensor ∇u and was defined as: $Q = 1/2(\Omega_{ij}\Omega_{ij} - S_{ij}S_{ij})$ [24]. Figure 3 shows an instantaneous snapshot of coherent structures with *BR* = 3.31 at t = 2.0*T*. We can observe all the dominant coherent structures: the horseshoe vortex appears just at the upstream of jet exit, the shear-layer vortices appear in the form of consecutive vortex rings, and the tornado-like wake vortices locate just behind the jet core. The hairpin vortices locate behind the jet exit, but they are a little bit difficult to be identified due to the high jet penetration in this case. Furthermore, hanging vortices also can be seen clearly. These vortices look like tubes and emerge directly above the jet orifice on the lateral edges of jet. Based on the opinion of Bidan and Nikitopoulos [4], the attached and detached jet regimes are identified at blowing ratios below 0.275 and above 0.6, respectively. They found that the latter case exhibited primary vortical structures of JICF. It is consistent with the simulation vortical structures under detached jet regime shown in fig. 3.
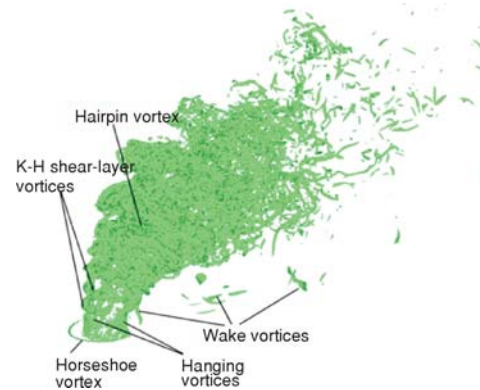
Figure 3. Instantaneous coherent structures with *BR* = 3.31 at constant of *t* = 2.0*T* (The coherent structures are identified by iso-surfaces of *Q* = 2.5)

Shangguan, Y., *et al.*: Large-Scaled Simulation on the Coherent Vortex ...

982   THERMAL SCIENCE: Year 2015, Vol. 19, No. 3, pp. 977-988
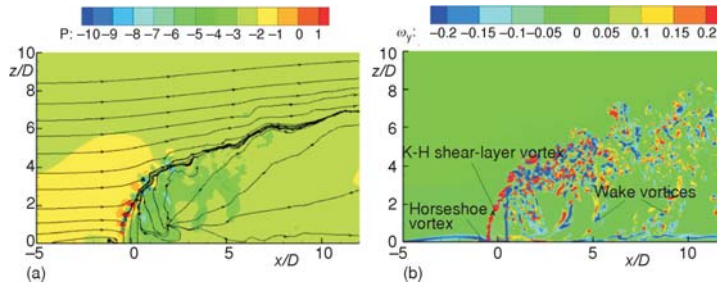
Figure 4. (a) Instantaneous non-dimensional pressure *P* contours attached with streamlines in the mid-span plane, and (b) instantaneous spanwise vorticity ω_y field in the mid-span plane
(for color image see journal web site)

Figure 4 displays the instantaneous flow characteristics with BR = 3.31 above the bottom plate in the mid-span plane (the plane of $y = 0$) at t = 2.0*T*. Figure 4(a) is pressure contours attached with streamlines, and the non-dimensional pressure is defined as $P = (p - p_\infty)/\rho u_\infty^2$. The spanwise vorticity ω_y field is in fig. 4(b). It is can be seen clearly that a high pressure region in the upstream of jet and an inverse pressure region on the trailing side of jet, fig. 4(a). The jet flow just likes a bluff body and makes the cross-flow stagnate causing the generation of upstream high pressure region. Moreover, the horseshoe vortex and the consecutive ring shear-layer vortices can be identified from the streamlines. It is obvious that the horseshoe vortex is formed near the stagnation point and the shear-layer vortices locate at the leading edge and trailing edge of jet hole. There is a separation point that appears in the area of adverse pressure distribution. At almost the same location as that of the point, the wake vortices occur fig. 4(b). This phenomenon indicates that the node, the separation of cross-flow boundary-layer, is the origin of wake vortices, which is consistent with the opinion proposed by Fric and Roshko [22]. Instantaneous vorticity field, fig. 4(b), shows the mixing due to K-H mode and the growth of flow structures as they are convected downstream. The anticlockwise vortices (vortices in red) with positive vorticity originate from the upper shear layer of jet flow, and the clockwise vortices (vortices in blue) are shed from the vorticity associated with the inner jet shear layer. The clockwise and anticlockwise vortices wrapping around jet core are convected about 2D downstream and decay.

The instantaneous spanwise vorticity field of $BR = 0.25$ at mid-span plane is illustrated in fig. 5. Unlike the results under detached jet regime (BR = 3.31), the vortices with positive vorticity (vortices in red) shedding from the leading edge of jet exit are prevailed over by the clockwise vortices (vortices in blue) fed by the cross-flow boundary layer. Because the vortex intensity of anticlockwise vortices (vortice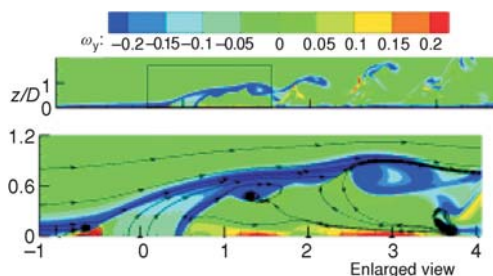s in red) shedding from the leading edge of jet hole is so weak due to the low blowing ratio. Then the clockwise vortices (vortices in blue) fed by the cross-flow boundary layer are transported downstream directly and turn into hairpin vortices, which can be observed in the enlarged view of spanwise vorticity field shown in fig. 5. However, the strong jet shear-layer vortices at the leading edge of jet hole in the case of $BR = 3.31$ lead the clockwise vortices (vortices in blue) associated with the cross-flow boundary layer to be stagnated ahead of the jet hole and the upper shear-layer vortices grow into horseshoe vortices (fig. 4). The strong penetration of

Figure 5. The instantaneous spanwise vorticity ω_y field with *BR* = 0.25 in the mid-span plane at $t = 2.0T$ (for color image see journal web site)

jet flow under the detached jet regime results in the strong anticlockwise vortices (vortices in red) shedding from the leading edge of jet hole. It is because that the large velocity gradient in the upper shear layer favors the formation of anticlockwise vortices. The clockwise vortices associated with the cross-flow boundary layer undergo a strong vorticity cancellation and are defeated by the strong anticlockwise vortices. Finally, the horseshoe vortex could hardly move downstream and remains near the leading edge of jet exit. The upper jet shear-layer vortices mix with the inner jet shear-layer vortices and give rise to the generation of hairpin vortex. All the observations suggest that the hairpin vortices in the case of $BR = 0.25$ (the attached jet regime), are mainly originated from the clockwise vortices related to the cross-flow boundary layer. While, the hairpin vortices under the detached jet regime primarily result from the anticlockwise vortices fed by the jet shear-layer. In the early research on JICF in 1999 [2], however, Yuan *et al.* proposed that the hairpin vortex originated from hanging vortices forming in the skewed mixing layers on each lateral edge of the jet with the computation of about 10^6 grids. Experimental work performed by Kelso *et al.* in 1996 [23] suggested that hairpin vortex developed in the jet shear layer just above the orifice by studying JICF with the blowing ratios ranging from 2.0 to 6.0.

   The features of coherent structures in JICF with $BR = 0.25$ at the constant of $t = 2.0T$ are shown in fig. 6. Coherent structures identified by iso-surface of $Q = 2.5$ colored by streamwise vorticity ω_y, spanwise vorticity ω_y and non-dimensional eddy viscosity v_t/v_0 are illustrated in fig. 6(a), (b), and (c), respectively. It is obvious that two protrusions lie just behind jet hole which are of the same streamwise and spanwise vorticity as that of horseshoe vortex. All of them have rearward swept legs. We believe that the horseshoe vortex formed in the front of jet hole convects downstream and grows into the protrusion. This idea have been proved by Bidan and Nikitopoulos [4]. It also can be observed from fig. 6(a) and (b) that the heads of hairpin vor-
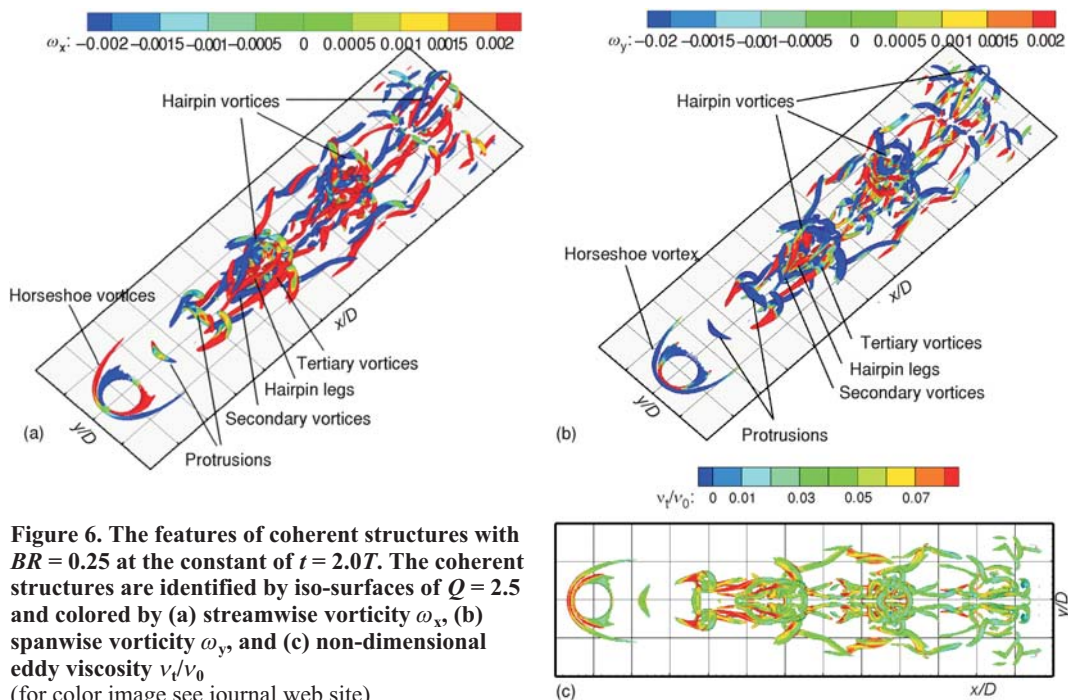

Figure 6. The features of coherent structures with $BR = 0.25$ at the constant of $t = 2.0T$. The coherent structures are identified by iso-surfaces of $Q = 2.5$ and colored by (a) streamwise vorticity ω_x, (b) spanwise vorticity ω_y, and (c) non-dimensional eddy viscosity v_t/v_0
(for color image see journal web site)

tex and horseshoe vortex are of the same sign in ω_x and ω_y. The rearward legs of horseshoe vortices move slower than their heads when vortices travel downstream and develop as the hairpin vortices with forward legs, due to the strong eddy viscosity in the adjacent of bottom plate displayed in fig. 6(c). This further approves that the horseshoe vortex (*i. e.* the cross-flow boundary layer vortex) is the original form of the hairpin vortex under the attached jet regime.

Owing to the simulation with high resolution, a pair of secondary vortices lying on the outside of the hairpin legs and a pair of tertiary vortices on the outboard of secondary vortices are captured. It is found that the values of ω_x and ω_y for the secondary vortices and the hairpin legs are of opposite sign. For the tertiary vortices, while, ω_x and ω_y have the same sign as those of the hairpin legs. These indicate that the secondary vortices are induced and strengthened by the rotation of hairpin legs, and the streamwise rotation of secondary vortices induces the tertiary vortices. This means that the secondary and tertiary vortices enhance the mixing process in JICF.

Capturing the coherent structures fine enough is necessary to know more about the interaction of fluids and put it into perspective. However, the fine coherent structures are difficult to be depicted due to limited computing resources. The computed results present not only the primary coherent structures but also the secondary and tertiary vortices. As far as we know, there are a few of published papers presenting the detailed coherent structures on account of the insufficient computational grids [25]. The present paper obtains the fine coherent structures efficiently with large-scaled simulation using LBM and multi-GPU, which has the profound meaning on further understanding of the complex mixing mechanism in JICF.

Mean flow results

A comparison between our simulation and the experiment of Ozcan *et al.* [14] is conducted under the condition of Re = 2400 and *BR* = 3.31. Figure 7 shows the profiles of mean (1) streamwise and (2) wall-normal velocity components in the mid-span plane ($y = 0$) at various locations near the jet hole (a) $x/D = -1.0$, (b) $x/D = -0.5$, and (c) $x/D = 0.5$. In the profiles, solid lines and deltas represent the results of our simulation and the experimental data [14], respectively. The profiles are plotted *vs.* the normal distance from the bottom plate. The normal distance are normalized by the jet hole diameter D, and the velocities are normalized by the cross-flow velocity u_∞. We pay more attention to the vicinity of jet exit, since many interesting phenomena occur in this area. It is shown that the results of our simulation agree reasonably with the experimental data.

As for the velocity distribution of streamwise component u at $x/D = -1.0$, fig. 7(1)(a), it is almost the same as the steady mean turbulent flat-wall boundary profile without considering the small twist nearby $z = 1.6D$. A small back-flow in the wall-normal velocity w profile appears in the range of $z \leq 1.6D$, as displayed in fig. 7(2)(a). This is because there is only a small streamwise vortex near the bottom plate changing the raw trend of velocities profiles. At $x/D = -0.5$, the leading edge of jet exit, the streamwise velocity u distribution, fig. 7(1)(b) is also similar to the steady mean turbulent flat-wall boundary profile except the small back-flow adjacent to the bottom plate. Although the experimental results showed the negative velocity areas in u distribution at $x/D = -0.5$, they did not depict the fluctuations that our simulation capture. This is in part due to the difference of the inflow condition between the computation and experiment, which has a great influence on the flow downstream of the entrance boundary [26]. At $x/D = 0.5$, the trailing edge of jet exit, the trend in the profiles of mean velocity is changed much by the emphasized interaction between jet flow and cross-flow. The velocity in wall-normal di-
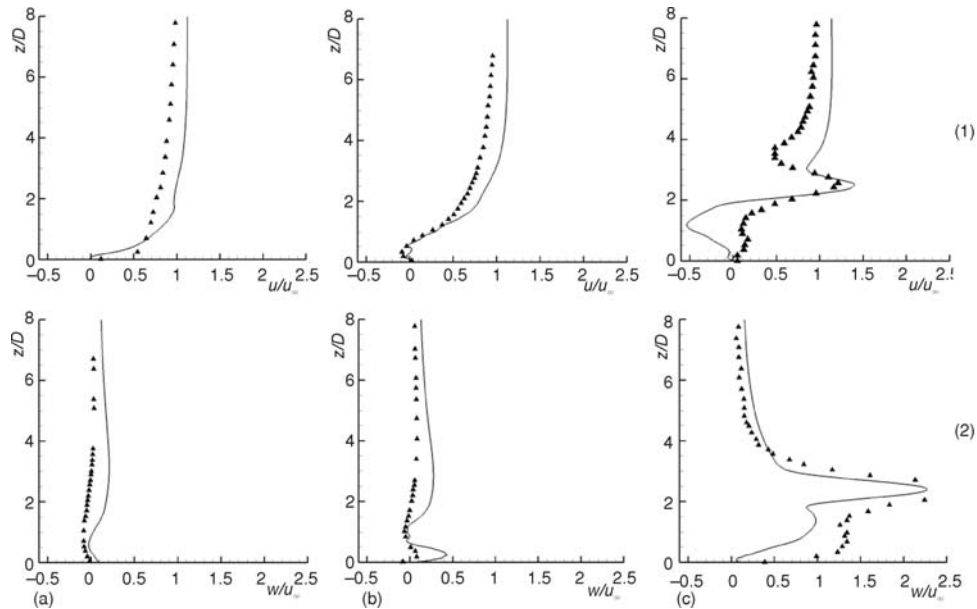
Shangguan, Y., *et al.*: Large-Scaled Simulation on the Coherent Vortex ...
THERMAL SCIENCE: Year 2015, Vol. 19, No. 3, pp. 977-988

985

Figure 7. The profiles of mean (1) streamwise and (2) wall-normal velocity components with BR = 3.31 in the mid-span plane at various locations near the jet exit; (a) *x/D* = –1.0, (b) *x/D* = –0.5 and (c) *x/D* = 0.5 (solid lines – results of LBM-LES computation, deltas – results of Ozcan and Larsen [14])

rection w exhibits two peaks. The outer maximum with the value of $2.30\ u_\infty$, which is 0.69 times of jet velocity u_j, is the symbol of jet core. Interestingly, all the trend changes appear within the turbulent boundary layer ($z \le 2.9D$). The phenomenon implies that in the area of $–0.5 \le x/D \le 0.5$, where the jet exhausts, the area affected by interaction of fluids does not exceed the turbulent boundary layer.

Figure 8 displays the profiles of (a) mean streamwise and (b) wall-normal velocity components, respectively, in the mid-span plane near the jet exit for the case of $BR = 0.25$. The interaction-affected area is smaller than that of the above case because of the weak jet-flow penetration with low jet velocity. Just at the leading edge of jet exit ($x/D = –0.5$), the streamwise ve-

locity profile with $BR = 0.25$ also shows a reverse flow zone near the bottom plate implying the horseshoe vortex with negative ω_y. At the trailing edge of jet exit, $x/D = 0.5$, the wall-normal velocity profile with $BR = 0.25$ presents the similar 'M' form as that of $BR = 3.31$. It is the inner maximum not the outer maximum that represents the core of jet, and the value of maximum w is about $0.85\ u_j$. All of these indicate that the weak penetration under the attached jet regimes leads to a small loss of jet momentum in wall-normal direction.
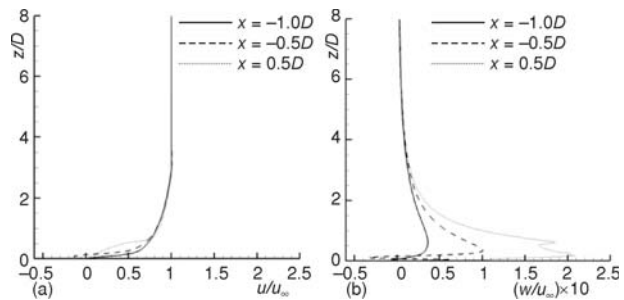

Figure 8. The profiles of mean (a) streamwise and (b) wall-normal velocity components in the mid-span plane ($y = 0$) at various locations near the jet exit under the case of $BR = 0.25$

986

Shangguan, Y., *et al.*: Large-Scaled Simulation on the Coherent Vortex ...
THERMAL SCIENCE: Year 2015, Vol. 19, No. 3, pp. 977-988

Figure 9 presents the profiles of r. m. s fluctuations corresponding to (1) streamwise and (2) wall-normal velocity in the mid-span plane at various locations near the jet exit under the case of (a) $BR = 3.31$ and (b) $BR = 0.25$. Apparently, all the turbulent quantitative results with $BR = 3.31$ are two orders of magnitude larger than that of $BR = 0.25$. It is implied that the high jet velocity under the detached jet regime makes the jet flow penetrate fast and deeply into the cross-flow leading to strong turbulence. It is found that cross-flow with $BR = 0.25$ influences the jet flow at the leading edge of jet exit ($x = -0.5D$) more significantly than jet flow at the trailing edge ($x = 0.5D$). In the case of $BR = 3.31$, however, the impact of cross-flow at the trailing edge of jet exit is greater than that of leading edge. The phenomenon reveals that jet flow in the detached jet regime is hardly affected by the cross-flow. It is also indicated quantitatively that the evolution mechanism of vortical structures is not constant, but varies with the different jet regimes.
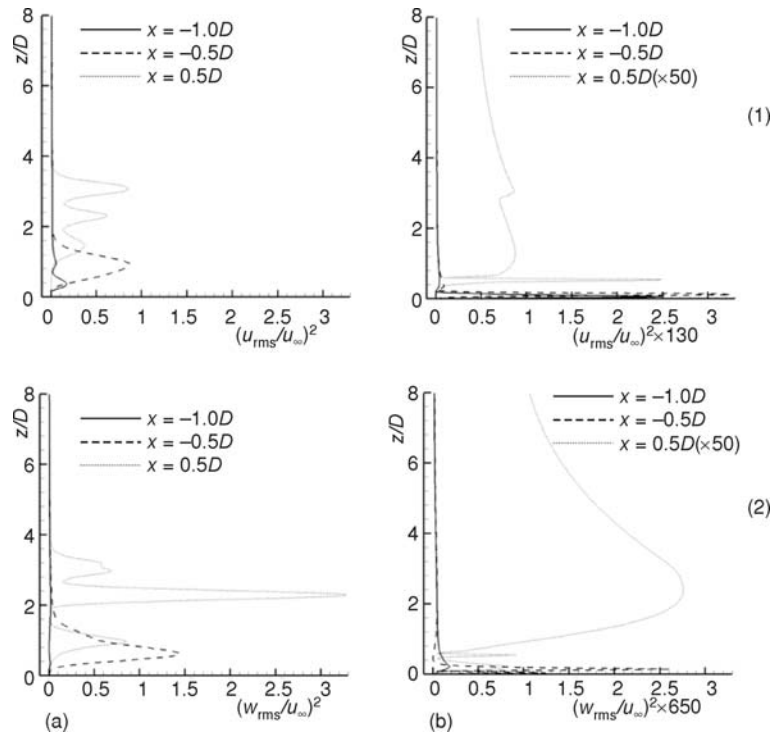

**Figure 9. The profiles of r. m. s fluctuations corresponding to (1)
streamwise and (2) wall-normal velocity in the mid-span plane at various
locations near the jet exit under the case of (a) $BR = 3.31$ and (b) $BR = 0.25$**

Conclusions

Large-scaled simulations on JICF are carried out by using LBM and multi-GPU, focusing on the difference of flow characteristics under attached and detached jet regimes. The detailed features of JICF are illustrated, containing the evolution characteristics of vortical system and the time-averaged flow results.

From the simulation results, it can be concluded that:

Shangguan, Y., *et al.*: Large-Scaled Simulation on the Coherent Vortex ...
THERMAL SCIENCE: Year 2015, Vol. 19, No. 3, pp. 977-988

987

- From the perspective of qualitative and quantitative, it is confirmed that the evolution mechanism of vortical system is not constant, but varies with the different jet regimes. Under the attached jet regime, the origin of hairpin vortex is cross-flow boundary layer vortex, while, the hairpin vortex in the case of detached jet originates from jet shear-layer vortex.
- The secondary vortices and the tertiary vortices locating on the outside of hairpin legs are captured with the high-resolution computation. It is found that these vortices can enhance the mixing process in JICF.
- The mean velocities obtained by the simulation coincide with the experimental results [14] in general indicating the good ability of LBM to compute flow physics in JICF. The mean velocities results also imply that the area affected by interaction of cross-flow and jet flow is not beyond the turbulent boundary layer in jet exhausts region ($-0.5 \leq x/D \leq 0.5$). Furthermore, the large loss of jet momentum in detached jet caused by the strong penetration also can be shown by the quantitative results.

Acknowledgments

Nomenclature

BR – blowing ratio, [–]
C_S – Smagorinsky constant, [–]
D – diameter of jet hole, [m]
$\vec{e}$ – particle velocity of LBE, [–]
f – particle velocity distribution function of LBE, [–]
f^{eq} – equilibrium particle velocity distribution function of LBE, [–]
L – the dimension of computational domain, [m]
N – velocity number of LBE, [–]
p – pressure, [Nm^{-2}]
Q – Q-criterion [$= 1/2(\Omega_{ij}\Omega_{ij} - S_{ij}S_{ij})$], [–]
Re – Reynolds number ($= UD/\nu$), [–]
S_{ij} – strain rater tensor, [m^{2}s^{-2}]
T – throw-time ($= L_x/u_\infty$), [s]
t – physical time, [s]
$\bar{u}$ – streamwise velocity, [ms^{-1}]

w – wall-normal velocity, [ms^{-1}]
x, y, z – Cartesian co-ordinates

Greek symbols

Δ_x – filter length scale, [–]
λ – the relaxation time of LBE, [s]
ν – viscosity, [Pa·s^{-1}]
ρ – density, [kgm^{-3}]
τ – non-dimensional relaxation time of LBE, [–]
ω – vorticity, [m^{2}s^{-1}]
ϖ – weighting factors of LBE, [–]
Ω_{ij} – rotation rater, [m^{2}s^{-2}]

Subscripts

j – jet flow
∞ – cross-flow

References

[1] Andreopoulos, J., Rodi, W., Experimental Investigation of Jets in a Cross-Flow, *Journal of Fluid Mechanics, 138* (1984), pp. 93-127
[2] Yuan, L. L., *et al.*, Large-Eddy Simulations of a Round Jet in Cross-Flow, *Journal of Fluid Mechanics, 379* (1999), pp. 71-104
[3] Yao, Y., *et al.*, Direct Numerical Simulation of Jets in Cross-Flow, *International Journal Computational Fluid Dynamics, 20* (2007), pp. 279-285
[4] Bidan, G., Nikitopoulos, D. E., On the Steady and Pulsed Low-Blowing-Ratio Transverse Jets, *Journal of Fluid Mechanics, 714* (2013), pp. 393-433
[5] Lawal, M. S., *et al.*, CFD Predictions of Wake-Stabilised Jet Flames in a Cross-Flow, *Energy, 53* (2013), pp. 259-269
[6] Brinkerhoff, J. R., Yaras, M. I., Direct Numerical Simulation of a Square Jet Ejected Transversely into an Accelerating, Laminar Main Flow, *Flow Turbulence and Combustion, 89* (2012), 4, pp. 519-546

[7]   Duda, B. M., *et al*., Application of the Scale-Adaptive Simulation to a Hot Jet in Cross Flow, *AIAA Journal, 51* (2012), 3, pp. 674-685
[8]   Andrew, D., *et al*., Evaluation of Massively-Parallel Spectral Element Algorithm for LES of Film-Cooling, *Proceedings*, Turbine Technical Conference and Exposition GT2013, San Antonio, Tex., USA, 2013
[9]   Miguel, A. F., Non-Darcy Porous Media Flow in No-Slip and Slip Regimes, *Thermal Science, 16* (2012), 1, pp. 167-176
[10]   Jourabian, M., Lattice Boltzmann Simulation of Melting Phenomenon with Natural Convection from an Eccentric Annulus, *Thermal Science, 17* (2013), 3, pp. 877-890
[11]   Sajjadi, H., Kefayati, R., Lattice Boltzmann Simulation of Turbulent Natural Convection in Tall Enclosures, *Thermal Science, 19* (2015), 1, pp. 155-166
[12]   Chen, S., Doolen, G. D., Lattice Boltzmann Method for Fluid Flows, *Annual Review of Fluid Mechanics, 30* (1998), pp. 329-364
[13]   Buck, I., *et al*., Brook for GPUs: Stream Computing on Graphics Hardware, *ACMT Graphic, 23* (2004), 3, pp. 777-786
[14]   Ozcan, O., Larsen, P. S., Laser Doppler Anemometry Study of a Turbulent Jet in Crossflow, *AIAA Journal, 41* (2003), 8, pp. 1614-1616
[15]   Cercignani, C., *Theory and Application of the Boltzmann Equation*, Scottish Academic Press, Edinburgh, UK,1975
[16]   Bhatnagar, P. L., *et al.*, A Model for Collision Processes in Gases. I. Small Amplitude Processes in, Charged and Neutral One-Component Systems, *Physics Review, 94* (1954), 3, pp. 511-525
[17]   Somers, J. A., Direct Simulation of Fluid Flow with Cellular Automata and the Lattice-Boltzmann Equation, *Applied Scientific Research, 51* (1993), 1-2, pp. 127-133
[18]   Hou, S., *et al*., A Lattice Boltzmann Subgrid Model for High Reynolds Number Flows, *Pattern Formation and Lattice Gas Automata, 6* (1996), pp. 151-168
[19]   Wang, X., *et al*., Direct Numerical Simulation and Large Eddy Simulation on a Turbulent Wall-Bounded Flow Using Lattice Boltzmann Method and Multiple GPUs, *Mathematical Problems in Engineering*, 2014 (2014), ID 742432
[20]   Bardina, J., *et al*., Effect of Rotation on Isotropic Turbulence – Computation and Modeling, *Journal of Fluid Mechanics, 154* (1985), pp. 321-336
[21]   Wang, X., Aoki, T., Multi-GPU Performance of Incompressible Flow Computation by Lattice Boltzmann Method on GPU Cluster, *Parallel Computing, 37* (2011), 9, pp. 521-535
[22]   Fric, T. F., Roshko, A., Vortical Structure in the Wake of a Transverse Jet, *Journal of Fluid Mechanics, 279* (1994), pp.1-47
[23]   Kelso, R. M., *et al*., An Experimental Study of Round Jets in Cross-Flow, *Journal Fluid Mechanics, 306* (1996), pp. 111-144
[24]   Hunt, J. C. R., *et al.*, Eddies, Streams, and Convergence Zones in Turbulent Flows, Report No. 88, Stanford University, Stanford, Cal., USA, 1988
[25]   Coussement, A., *et al*., Large Eddy Simulation of a Plused Jet in Cross-Flow, *Journal of Fluid Mechanics, 695* (2012), pp. 1-34
[26]   Guo, X., *et al*., Large-Eddy Simulations of Film Cooling Flows, *Computers & Fluids, 35* (2006), 6, pp. 587-606